

Turbo-GS: Accelerating 3D Gaussian Fitting for High-Quality Radiance Fields

Tao Lu^{*1} Ankit Dhiman^{*2} R Srinath^{*2} Emre Arslan¹ Angela Xing¹
 Yuanbo Xiangli³ R Venkatesh Babu² Srinath Sridhar¹
¹Brown University ²Indian Institute of Science, Bangalore ³Cornell University

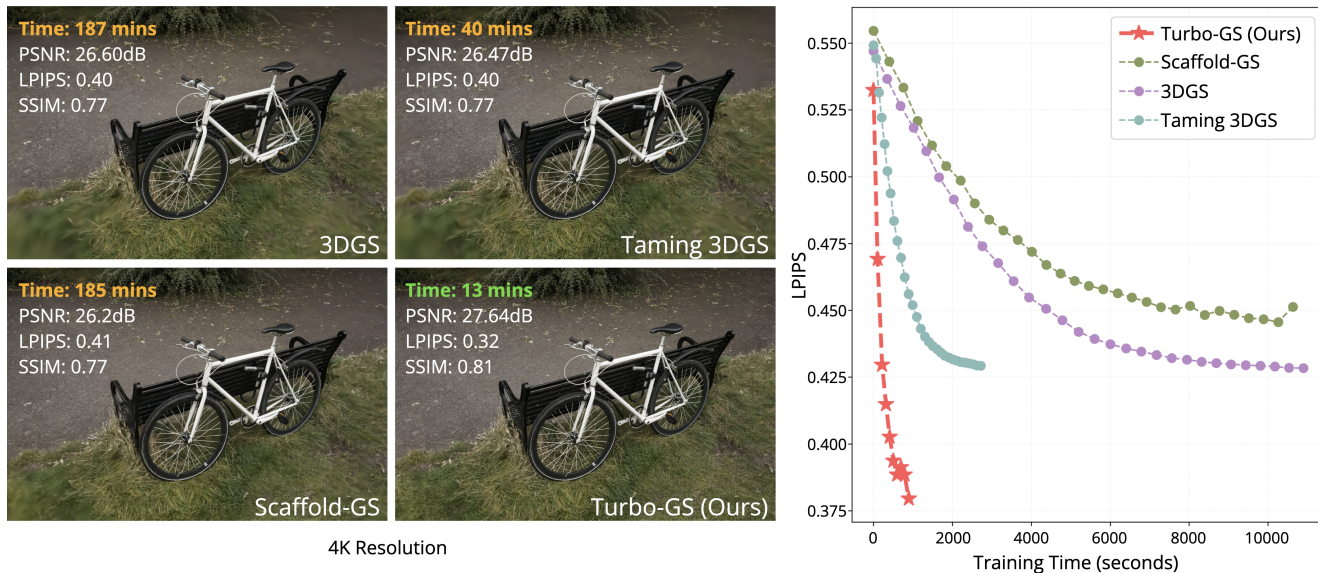


Figure 1. **Turbo-GS** accelerates 3DGS fitting significantly while preserving rendering quality. It proposes efficient densification strategy and innovative dilated rendering allow training on 4K images in minutes—significantly outperforming baseline methods. Notably, Turbo-GS converges on the 4K bicycle scene in just **13 minutes**—over **3×** faster than Taming 3DGS (40 minutes), **14×** faster than 3DGS (187 minutes) and Scaffold-GS (185 minutes).

Abstract

Novel-view synthesis is an important problem in computer vision with applications in 3D reconstruction, mixed reality, and robotics. Recent methods like 3D Gaussian Splatting (3DGS) have become the preferred method for this task, providing high-quality novel views in real time. However, the training time of a 3DGS model is slow, often taking 30 minutes for a scene with 200 views. In contrast, our goal is to reduce the optimization time by training for fewer steps while maintaining high rendering quality. Specifically, we combine the guidance from both the position error and the appearance error to achieve a more effective densification. To balance the rate between adding new Gaussians and fitting old Gaussians, we develop a convergence-aware budget control mechanism. Moreover, to make the densification process more reliable, we selec-

tively add new Gaussians from mostly visited regions. With these designs, we reduce the Gaussian optimization steps to one-third of the previous approach while achieving a comparable or even better novel view rendering quality. To further facilitate the rapid fitting of 4K resolution images, we introduce a dilation-based rendering technique. Our method, **Turbo-GS**, speeds up optimization for typical scenes and scales well to high-resolution (4K) scenarios on standard datasets. Through extensive experiments, we show that our method is significantly faster in optimization than other methods while retaining quality. Project page: <https://ivl.cs.brown.edu/research/turbo-gs>.

1. Introduction

Building the radiance field [31] of a scene from multiple posed RGB images has recently become an important problem in computer vision given numerous applications in photorealistic novel view synthesis (NVS) [1,

*Equal Contribution.

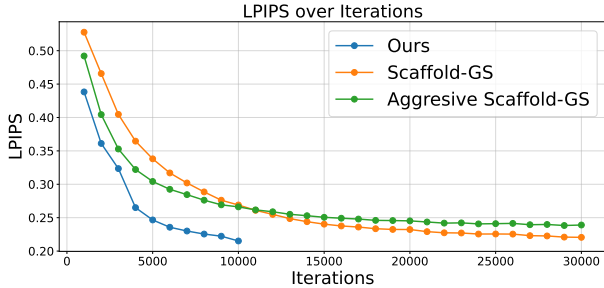


Figure 2. **Effect of Densification Rate.** This plot shows the effect of densification rate with Scaffold-GS [29] versus Turbo-GS (Ours) on the Bicycle scene [1]. Scaffold-GS with densification every 100 iterations (default, orange) takes time to converge. An aggressive version of Scaffold-GS with densification every 20 iterations (green) initially shows improved convergence, but plateaus afterward. Ours (blue) produces higher-quality reconstruction with densification every 20 iterations.

15, 24, 29, 33], 3D reconstruction [18, 43], mixed reality [7], and robotics [6, 48]. While radiance fields were initially represented *implicitly* using a neural network [1, 31], primitive-based *explicit* methods have become more popular [3, 15, 45]. In particular, 3D Gaussian Splatting (3DGS) [24], a method that uses 3D Gaussian primitives, has become the method of choice for representing radiance fields. 3DGS generates high-quality novel views by using a differentiable renderer based on Gaussian splat rasterization, achieving real time rendering rates for 1080p (1K) images on a GPU.

Despite the progress in the NVS quality and rendering times, *fitting (or optimizing)* a high-quality radiance field from posed images remains slow. For example, using 3DGS to fit a static scene with 200 camera views at 1K resolution might take anywhere from 30 minutes to several hours, depending on the scene. This poses a significant challenge to the widespread adoption of radiance fields in broader problems, including modeling dynamic scenes and semantics.

Some prior works have recognized this problem and proposed solutions. For example, learning-based methods [11, 50, 52] estimate intermediate Gaussian initializations or directly estimate the final Gaussian positions in a feed-forward manner, enabling reconstruction in a few seconds. However, these methods are limited to a fixed number of input views and their generalization abilities are not well studied. Among learning-free methods that can handle an arbitrary number of views, the focus has been on building highly-optimized CUDA implementations [30], lightweight encodings to quantize Gaussian attributes [16], or replacing the optimizer with second-order methods for quicker convergence [20]. These methods speed up optimization, but more improvements are needed, especially for high-resolution 4K images.

We focus on accelerating the per-scene optimization of

3DGS *without using any learning-based prior and without sacrificing quality*. A typical 3DGS pipeline consists of several components and design choices that directly impact fitting time: (1) **optimizer-related** components include initialization, optimizer choice, optimization scheduler, and number of iterations, and (2) **non-optimizer** components include the number of Gaussians, the rasterizer, Gaussian densification and pruning, and post-processing. Previous work speeds up a subset of these components, for instance, the optimizer [20] or the backward process [30]. Further improvements appear feasible, but have not yet been explored.

In this paper, we introduce **Turbo-GS**, a method for fitting 3DGS that is **several times faster** than current state-of-the-art methods while matching or surpassing the quality of novel view synthesis. While existing methods [30] focus on reducing the time for one optimization step, we focus on *reaching a higher quality with fewer steps*. This is challenging since previous methods require a high number of iterations with a low *densification rate* – the interval after which 3D Gaussians are split. As shown in Figure 2 (green), increasing the densification rate results in early gains, but it eventually plateaus. Moreover, the initialization of the Gaussians has a big impact on the number of steps needed.

Targeting the aforementioned issues, we contribute a series of designs that quickly stabilize the process and allow higher densification rates. First, the existing densification method [24] relies solely on Gaussian positional error but ignores appearance, resulting in poor performance in texture-less areas. We introduce **position-appearance guidance** for more effective densification. Second, to balance densification and Gaussian fitting quality, we propose a **convergence-aware budgeting** process for adding new Gaussians. Finally, we make densification more reliable using an adaptive mechanism that **selectively adds Gaussians** only to the most frequently visited regions. In addition, we bootstrap optimization by initializing with an upsampled SfM point cloud [38], and use a batched training strategy to reduce gradient oscillations.

With these contributions, Turbo-GS matches or outperforms the rendering quality of existing methods using only a third of the optimization steps. When combined with a dilation-based rendering approach that decomposes the learning content from low to high frequency, we can even accelerate optimization for high-resolution 4K images (Figure 1). We conduct extensive experiments to validate our design choices and compare our approach with previous methods. To sum up our contributions:

- We propose **Turbo-GS**, a method for fitting 3DGS that is several times faster than existing methods. Our key idea is to reduce the number of optimization iterations while enabling more frequent and effective densification.
- We make a series of design contributions to achieve frequent and effective densification, better initialization, and

stabilize gradients during fitting.

- A series of other improvements, including a batching strategy, and dilation-based rendering for 4K images.

2. Related Work

2.1. Novel View Synthesis

Novel-view synthesis has gained significant traction in recent years, with Neural Radiance Fields (NeRF) [31] emerging as a standout technique for generating highly photorealistic images. NeRF achieves this by leveraging volume rendering to optimize multi-layer perceptron (MLP) weights, but the original approach is computationally expensive and requires several hours or even days for training. To address this, subsequent works have integrated NeRF with explicit representations like voxel and feature grids [15, 23, 39, 41], hash grids [32], and point-based methods [42] to dramatically accelerate training times.

3D Gaussian Splatting (3DGS) [24] extends these developments by modeling scenes as a collection of 3D Gaussians that are projected as 2D splats and combined using alpha blending to form pixel colors. This technique has gained popularity for enabling high-quality, real-time rendering. Scaffold-GS [29] further enhanced 3DGS by introducing a hierarchical structure that aligns anchors with scene geometry. They introduced a multi-resolution error-based densification strategy that further enhances the robustness of the adaptive control of Gaussians, improving both rendering quality and memory efficiency. Meanwhile, numerous works have focused on various enhancements to 3DGS, including improved rendering quality [21, 47], faster rendering [9, 16], level-of-details [37], better surface reconstruction accuracy [17, 46], memory optimization [36], and the ability to handle large-scale scenes [25]. While 3DGS delivers high-quality results with extremely fast rendering, it faces challenges such as unpredictable storage requirements and variable fitting durations, which can hinder its effectiveness in downstream applications.

2.2. Accelerating Gaussian Splatting Fitting

Recognizing the limitation in fitting speed, some recent work has focused on accelerating fitting and improving efficiency by enhancing initialization methods [14, 22, 26, 35], optimizing Gaussian budget (number of Gaussians) allocation [12, 30], and reducing overall training time [16, 20, 34].

In terms of initialization, methods such as Rain-GS [22] and Gaussian Splatting as MCMC [26] enable effective model fitting from sub-optimal, or randomly initialized point clouds, expanding the robustness of 3DGS in diverse settings. CoherentGS [35] leverages monocular depth and dense flow correspondences to provide a well-defined set of initial 3D Gaussians, while studies exploring alternatives to SfM-based initialization [14] have shown that com-

binning improved random initialization with NeRF’s structural guidance achieves, or even surpasses, the quality of COLMAP initialization on large-scale, challenging scenes.

In managing the Gaussian budget, Mini-Splatting [12] identifies spatial inefficiencies within Gaussian distributions and introduces strategies like blur splitting, depth reinitialization, and intersection-preserving sampling to address these redundancies. Taming 3DGS [30] extends this approach by adapting Gaussian distribution to specific use cases while prioritizing perceptual quality through a flexible, score-based framework. Efforts to reduce training time, including EAGLES [16] and Compact3D [34], use quantization to streamline storage and computation, while 3DGS-LM [20] replaces the Adam optimizer with the LM optimizer to accelerate convergence. Other works improve the optimization runtime by improving the implementation of the underlying differentiable rasterizer [8, 13, 44].

A line of research has also focused on sparse-view reconstruction using a data-driven, feed-forward approach, directly generating Gaussians in a single forward pass [2, 4, 5, 10, 49]. In this work, we do not rely on priors from large foundation models, as they have limited capability to accommodate densely captured views and generally cannot handle high-resolution scene modeling.

3. Preliminaries

In this section, we present a brief overview of 3DGS and related methods. Numerous previous works have tried to improve 3DGS along many dimensions, *e.g.*, 2DGS [21] for geometry, Mip-Splatting [47] for antialiasing and Scaffold-GS [29] for connecting the explicit and implicit 3D representation. We choose to build Turbo-GS on top of Scaffold-GS as it is already a step towards improved structure, compactness and efficiency, potentially benefiting our goal.

3D Gaussian Splatting. 3DGS [24] models scene geometry as a set of 3D Gaussian primitives. Each 3D Gaussian is formulated as:

$$G(x) = e^{-\frac{1}{2}(x-\mu)^T \Sigma^{-1}(x-\mu)}, \quad (1)$$

where μ is the center position and Σ is an anisotropic covariance matrix. To ensure they are positive and semi-definite, the covariance matrix is defined by a rotation matrix R and scaling matrix S as $RSS^T R^T$. Additionally, each Gaussian has an opacity parameter σ and spherical harmonics (SH) coefficients to model view-dependent color. To render a given viewpoint, the Gaussians are projected as 2D splats, sorted by depth, and combined with α -blending using a tile-based rasterizer. The color C of each pixel is defined by:

$$C(x') = \sum_i c_i \sigma_i \prod_{j=1}^{i-1} (1 - \sigma_j), \quad \sigma_i = \alpha_i G'_i(x'), \quad (2)$$

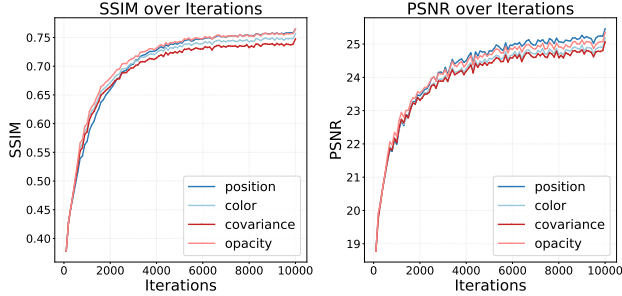


Figure 3. **Different Gradients Schema.** We find that covariance-based densification yields subpar quality; and in practice, opacity-based densification always leads to floaters. Color and position gradients are more reliable.

where x' is the queried pixel, c_i is the color of the i -th Gaussian, α_i is the learned opacity for the i -th Gaussian, and $G'_i(x')$ is the 2D projection of the Gaussian at pixel x' . 3DGS begins with a sparse SfM point cloud and optimizes by minimizing the loss (a combination of \mathcal{L}_1 and SSIM loss) between the rendered and ground truth images. Gaussians with low opacity are pruned, and new Gaussians are added in areas with high gradients.

Scaffold-GS. Scaffold-GS [29] introduces a hierarchical, structured approach to model a scene by introducing anchor points. Each visible anchor at point x_v spawns k neural Gaussians calculated by:

$$\{\mu_0, \dots, \mu_{k-1}\} = x_v + \{O_0, \dots, O_{k-1}\} \cdot l_v,$$

where $\{O_i\}$ represented the learnable offsets and l_v is the scaling factor associated with the anchor. Each neural Gaussian has attributes opacity α , color c , rotation q , and scale s that are computed using individual MLPs F_α , F_c , F_q , and F_s . For example, the opacity values of neural Gaussians are defined by:

$$\{\alpha_0, \dots, \alpha_{k-1}\} = F_\alpha(\hat{f}_v, \Delta_{vc}, \tilde{d}_{vc}),$$

where \hat{f}_v is the anchor feature, Δ_{vc} is the relative viewing distance, and \tilde{d}_{vc} is the direction between the camera and anchor. Neural Gaussians are then rasterized following [24]. Scaffold-GS initializes anchor points from SfM and optimizes learnable parameters and the MLPs using a loss function that combines \mathcal{L}_1 , SSIM loss, and volume regularization. Anchors with low opacity values are pruned while new anchors are added where the gradient of neural Gaussians exceeds a predefined threshold. In our method, we adopt Scaffold-GS because its structured management of Gaussians provides a more stable scene structure that is suitable for frequent Gaussian operations.

4. Turbo-GS: Accelerated 3D Gaussian Fitting

Our goal is to build a method for fitting 3D Gaussians that is significantly faster than existing work without compromis-



Figure 4. **Gradient Visualization.** We rasterize the Gaussian gradient into image plane and observe that: (a) Position Gradients focus only on certain regions in the scene, while (b) Color Gradients provide cues from overall regions. These are useful for regions such as grass and background structure.

ing radiance field quality. Unlike other methods that aim to minimize the footprint of each optimization step [20, 30], our key idea is to *reach high quality with fewer steps* by increasing the densification rate (Figure 2). We first describe our strategy for effective densification at a high rate (Section 4.1), followed by our initialization and dilated-rendering strategy for high resolution radiance fields.

4.1. Effective & Frequent Densification

Previous works [24, 29] split Gaussians in areas with strong positional gradients. However, this strategy fails in texture-less regions due to vanishing gradients, as shown in Figure 4, indicating that position-based densification strategy is suboptimal. To find a better densification criteria, we analyze the contribution of gradients from other Gaussian properties like covariance, opacity, and color. As shown in Figure 3, position-based densification exhibits slow convergence in the early stages, primarily due to local minima in texture-less regions. Although color-based densification converges faster, it struggles to accurately capture scene structure, resulting in overfitting to training views and poor convergence in later stages. Furthermore, we find that opacity and covariance-based densification strategies contribute little, with opacity-based densification even producing floaters. Thus, we opt to use a combination of color and position gradients as the criteria for our densification strategy, which also help effectively decouples scene appearance from geometry.

We further analyzed how position and color-based densification strategies impact different image regions. As shown in Figure 4, the position-based strategy generates weak gradient signals in texture-less areas since it does not account for color information. In contrast, the color-based strategy produces a strong signal in these areas. Therefore, using a color *and* position-based strategy achieve a more refined reconstruction to both the scene structure and appearance.

Position-Appearance Based Densification. Based on the above analysis, we design a densification method that combines the positional and appearance errors. We threshold

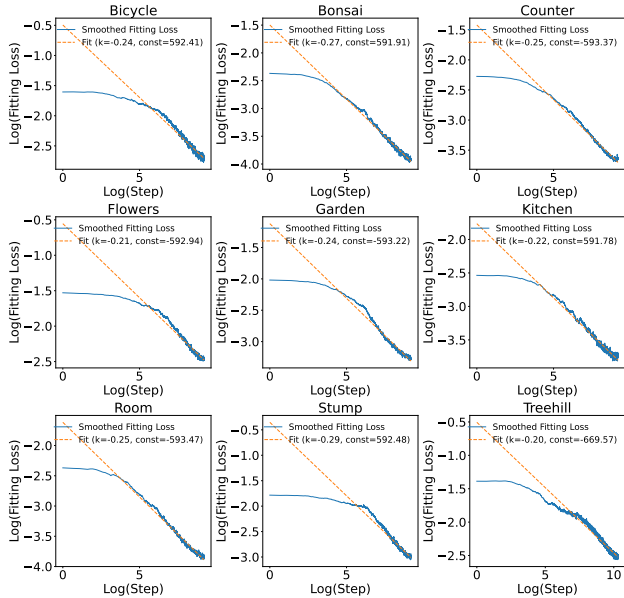


Figure 5. **Loss analysis with power function fitting.** For all scenes, the $\log(\text{loss})$ is linear to the $\log(\text{iterations})$ after the initial stage. Thus, the relation between iteration and convergence follows a power function. We design a power-law-based adaptive budget schedule based on these insights.

the position and appearance gradient with τ_{position} and τ_{color} respectively to determine whether densification is needed. We observe that the color gradient has a smaller numerical range, so we set $\tau_{\text{color}} = 0.01 * \tau_{\text{position}}$. Then, we follow Scaffold-GS’s [29] design to add points with multi-scale voxels. Since appearance-based densification tends to overfit, we only activate it with a probability of 20% to supplement the position-based densification. We find that the color branch improves reconstruction even if it is not frequently activated. To enhance the densification reliability, considering that the gradient from low opacity Gaussian are sensitive, we introduce an opacity-based masking strategy that excludes low-opacity Gaussians from contributing to densification decisions.

Convergence-aware Training Schedule. Denoting the initial number of Gaussian points as N , we manually set a maximum number M . The challenge then is how to grow from N to M . A proper budget mechanism to regulate newly added Gaussians helps control the growth rate of Gaussian and maximize improvement for reconstruction in each iteration.

To create such a budget, we take a closer look at how the reconstruction process converges. We calculated the log value of the training loss and iterations in Figure 5, and observed that after the initial stage, the $\log(\text{loss})$ is almost perfectly linear to the $\log(\text{iterations})$ in every scene (demonstrated on MipNeRF360 [1]). This means that the relation

between fitting iterations and model convergence follows a power function, which can be ascribed to the use of MSE loss [28] and L1 loss. Based on this finding, we design a power-law-based adaptive budget schedule.

Specifically, in a power-law dominated system, the loss is expected to follow a power function. Therefore, our goal is to check whether the newly added Gaussian points have caused the convergence process to deviate from the power law. Starting with an initial power exponent α_{base} , we record the loss at each iteration after 100 warm-up steps. Periodically, we fit a historical power exponent α_{history} using all recorded losses smoothed by exponential moving average. We then evaluate the loss over the most recent k iterations to compute a local power exponent α_{recent} . The difference $\epsilon = \alpha_{\text{recent}} - \alpha_{\text{history}}$ is used to adjust the power. The updated power is given by:

$$\alpha = \alpha_{\text{base}} + \lambda \cdot \tanh(\epsilon).$$

For simplicity, we set the α_{base} as the average value from historical α_{base} in our experiments, and we set $\lambda = 0.5$. Then, the budget $B(t)$ for iteration t is given by

$$B(t) = N + \frac{t^\alpha - 1}{100^\alpha - 1} * (M - N).$$

This balances the growing speed of new Gaussians and the optimization speed of old Gaussians. If the convergence speed is lower than the expectation from power law, we then slow down the densification, and vice versa.

Selective Densification. For more reliable densification, we use a selective strategy, where only Gaussians visited more than τ_v times are eligible to spawn new Gaussians. This ensures a lower bound on errors made when adding new Gaussians. However, the visit frequency between the foreground object and the background object varies significantly. Thus, the selective control could make it harder to grow new Gaussians in the background area. To balance this, we propose an adaptive threshold for the selection. Specifically, for a dataset with n views, we will count the visiting times v for each Gaussian in every n iterations. If $v < 5$, then we will turn down its threshold by half.

4.2. Initialization, Batching, & High Resolution

Better Initialization During initialization, to address the sparsity of the initial SfM point cloud, we employ a KD-tree-based densification technique. This method constructs a KD-tree from the sparse points and uses nearest-neighbor interpolation to generate additional points, effectively increasing the density of the original point cloud. By adaptively inserting new points between neighboring pairs, we create a denser representation that serves as a more robust foundation for subsequent training.

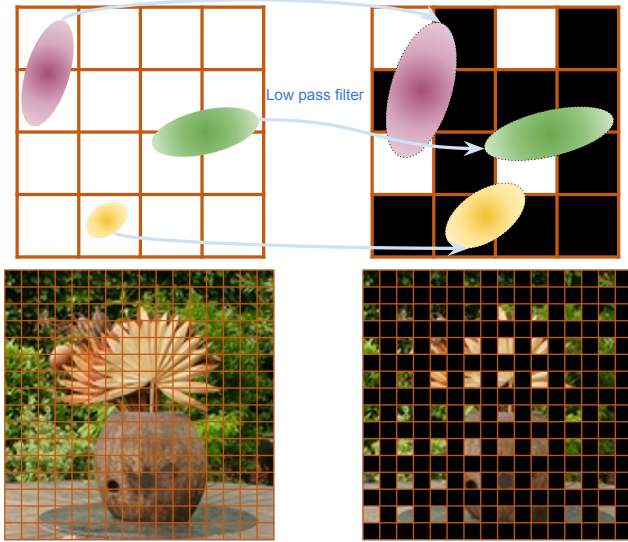


Figure 6. **Dilated Rendering.** Since each Gaussian affects multiple pixels in a view, dense pixel-wise supervision is redundant. Instead, we introduce a dilated rendering pipeline that selectively renders a subset of pixels in a chessboard pattern, which reduces the rendering burden while provide sufficient information for differentiable training.

Batched training To accelerate convergence in the final stage, we employ gradient accumulation across multiple iterations before updating the parameters. This approach reduces optimization noise, resulting in more stable and precise gradient directions. Empirically, we observed that batched training significantly improved performance during this final stage.

Handling High-Resolution Images. For extremely high-resolution training scenarios (*e.g.*, 4K images), training directly on full-resolution images is computationally intensive and memory inefficient. A common strategy is to begin training at a lower resolution and progressively upsample to higher resolutions. While effective, this approach can degrade rendering quality if the Gaussian model is trained with limited iterations. Given that Gaussian splatting employs a tile-based rendering approach, where each Gaussian typically influences multiple pixels, dense pixel-wise supervision often results in redundancy. Therefore, we propose to render a subset of pixels rather than the entire image.

Specifically, we introduce a dilated rendering pipeline that utilizes a chessboard sampling pattern (Figure 6). This chessboard pattern is controlled by three parameters: the dilation size and two offsets for width and height. Considering that the rasterizer initializes one thread per pixel in each tile, it can lead to underutilized resources during dilated rendering because fewer pixels are processed. To address this, we modify the thread-to-pixel mapping by re-

ducing the number of threads per block in line with the reduced pixel count. As a result, in the rendering kernel, each thread now performs alpha blending only for active pixels, eliminating idle threads. In this setup, each thread’s position corresponds to an active pixel, and thread ranks are adjusted to ensure pixel-wise outputs are consistently mapped to the same rank. This mapping guarantees consistency between the forward and backward passes. In the forward pass, an image is produced based on the dilation pattern, while the backward pass selectively skips invalid pixels according to this pattern, processing only the valid pixels per Gaussian.

Further, we apply a low-pass filter in the screen space to prevent any Gaussian from being restricted to a single pixel, thus avoiding any insufficient gradient updates. Denoting the covariance in the image plane as $\sigma \in \mathcal{R}^{2 \times 2}$, the diagonal elements are modified as:

$$\begin{cases} \sigma'_{0,0} = \sigma_{0,0} + 0.3 + 0.5(p - 1), \\ \sigma'_{1,1} = \sigma_{1,1} + 0.3 + 0.5(p - 1), \end{cases}$$

where p denotes the pattern size of the dilated sampling. In the densification phase, training is done exclusively using the dilated rendering. Post-densification, we randomly apply dilated rendering to reduce computational overhead. Experiments (Sec. 5.4) show that this approach maintains convergence stability.

5. Experiments

We present implementation details of the proposed method in Section 5.1. We discuss the benchmark datasets and baseline methods in Section 5.2. We present qualitative and quantitative results in Section 5.3. More details and results are available in the supplementary material.

5.1. Implementation Details

We build Turbo-GS on top Scaffold-GS [29], and we use the Taming 3DGS’s [30] optimized CUDA kernel for backward propagation. All of our experiments are trained for 10K iterations unless otherwise stated. In the first 3K iterations, we conduct densification for every 20 steps after 300 warm-up steps. All evaluations were conducted on a single NVIDIA RTX A6000 GPU.

5.2. Dataset and Baselines

We evaluate our method on all nine scenes of MipNeRF-360 [1] and two scenes of Deep Blending [19]. For MipNeRF-360, we downsample outdoor scenes by four and indoor scenes by two, as described in 3DGS [24]. For other scenes, we use the original resolution.

Metrics. We use standard quality metrics Peak Signal-to-Noise Ratio (PSNR), Structural Similarity (SSIM) [40] and Learned Perceptual Image Patch Similarity (LPIPS) [51].

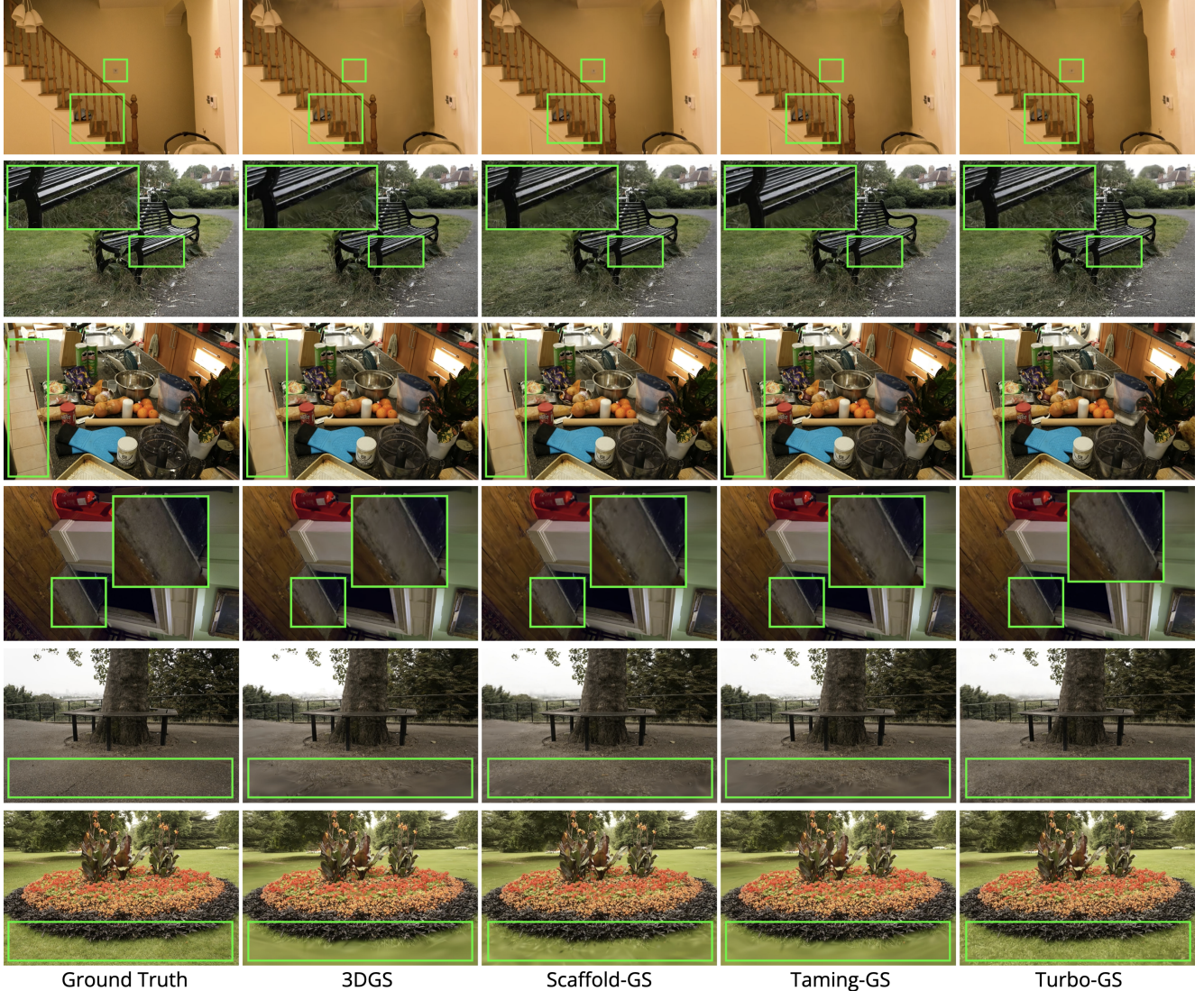


Figure 7. Qualitative comparison with prior 3DGS-based methods and the corresponding ground truth images from testing views. We obtain on-par or better results compared to 3DGS, Scaffold-GS, and Taming 3DGS, especially in high-frequency and texture-less areas highlighted in green: grass (second, last row), floor (fourth row) and pavement (fifth row).

Further, we also report the optimization time, memory and peak number of Gaussian primitives ($\#G$) during training.

Baselines. We compare our method with popular novel-view synthesis methods: 3DGS [24], ScaffoldGS [29] and MipNeRF-360 [1]. Since our goal is to speed up fitting, we also compare with works with similar goals such as Taming 3DGS [30], Mini-Splatting[12] and EAGLES [16]. We use the default settings in the paper for these baselines.

5.3. Results and Analysis

Quantitative Analysis. For quantitative analysis, we followed evaluation methodology proposed in 3DGS [24]. We observe that 3DGS takes on an average of ~ 30 minutes for MipNeRF-360 scenes in Table 1. Other 3DGS-based meth-

ods like EAGLES and Mini-Splatting are faster than 3DGS but take about ~ 20 minutes. Taming 3DGS is fast, but it still takes ~ 16 minutes on these challenging scenes. In contrast, Turbo-GS takes only ~ 5 minutes which is $3\times$ faster than Taming 3DGS and $5.6\times$ faster than 3DGS methods. In addition, we maintain similar or better quality than the other methods. The average training time of Turbo-GS for Deep Blending is ~ 3 minutes.

Qualitative Analysis. We compare our method qualitatively with 3DGS, Scaffold-GS, and Taming 3DGS in Figure 7. We observe that our method preserves finer details consistently. As shown in Figure 7, our method preserves

Table 1. Quantitative comparison with NeRF-based methods (top half) and 3DGS-based methods in (bottom half). We compare PSNR, SSIM, and LPIPS for quality. For resource efficiency, we report training time, memory and, where applicable and peak number (Peak #G) of Gaussians used. * denotes using Sparse Adam.

	MipNeRF-360 [1]						Deep Blending [19]					
	SSIM↑	PSNR↑	LPIPS↓	Train time ↓	Memory ↓	Peak #G ↓	SSIM↑	PSNR↑	LPIPS↓	Train time ↓	Memory ↓	Peak #G ↓
Instant-NGP [33] (Big)	0.699	25.59	0.331	7.50 m	48 MB	-	0.817	24.96	0.390	8.0 m	48 MB	-
Plenoxels [15]	0.626	23.08	0.463	25.82 m	2.1 GB	-	0.795	23.06	0.510	27.82 m	2.7 GB	-
3DGS [24]	0.814	27.45	0.217	30.08 m	640 MB	2.71 M	0.902	29.75	0.241	30.58 m	580 MB	2.46 M
Taming 3DGS [30]	0.814	27.46	0.218	15.78 m	628 MB	2.66 M	0.903	29.72	0.241	13.36 m	581 MB	2.46 M
Taming 3DGS* [30]	0.809	26.64	0.227	10.05 m	566 MB	2.39 M	0.902	29.65	0.248	8.12 m	543 MB	2.3 M
Mini-Splatting [12]	0.822	27.34	0.217	21.71 m	117 MB	4.23 M	0.908	29.90	0.253	18.05 m	83 MB	4.53 M
EAGLES [16]	0.807	27.09	0.234	22.22 m	57 MB	1.93 M	0.907	29.77	0.249	23.96 m	52 MB	1.96 M
Mip-Splatting [47]	0.828	27.64	0.188	41.47 m	1 GB	4.18 M	0.903	29.37	0.239	37.26 m	840 MB	3.49 M
Scaffold-GS [29]	0.814	27.71	0.221	23.85 m	180 MB	0.59 M	0.909	30.29	0.252	17.25 m	54 MB	0.18 M
Turbo-GS (Ours)	0.812	27.38	0.210	5.28 m	240 MB	0.49 M	0.910	30.41	0.239	3.24 m	174 MB	0.39 M

Table 2. Quantitative comparison on 3DGS-based methods for MipNeRF360-4K [1]. Turbo-GS (Ours) is not only fast but outperforms baseline methods in all the metrics.

	PSNR↑	SSIM↑	LPIPS↓	Train time
3DGS [24]	26.75	0.797	0.410	113 m
Taming 3DGS [30]	26.66	0.795	0.357	28 m
Scaffold-GS [29]	26.84	0.794	0.359	143 m
Turbo-GS (Ours)	26.98	0.808	0.323	12 m

fine details in regions such as grass (second and last row), pavement (fifth row) and floor (third row). In contrast, Taming 3DGS, which has a fast optimization time, is not able to preserve details in these regions. Turbo-GS is not only fast, but also preserves the high-frequency details.

5.4. Ablation Study

We present ablation studies on key design choices in our method. More ablations are in the supplementary material. All the ablation are conducted on the bicycle scene from MipNeRF360 [1].

Importance of Color-Gradient for densification. We show how cues from color gradients support position gradients during densification. We present two strategies: (1) position only and (2) position + color(p), where “ p ” denotes the probability of enabling color gradients, as shown in Table 3. While the position-only design achieves reasonable PSNR, it significantly affects image structure, as indicated by a low LPIPS score. In contrast, introducing color gradients improves LPIPS, validating the effectiveness of the proposed densification strategy. We observe that the color-gradient’s frequency has little impact on quality.

Impact of dilated rendering. We compare dilated rendering with the multi-scale training policy in Table 4. We observe that compared to full-resolution training, multi-scale has a significant drop; 0.22 dB in PSNR and 0.021 drop in LPIPS. In contrast, our dilated rendering training

Table 3. Ablation on importance of color gradients in densification strategy for Bicycle [1]. p denotes the probability of enabling color gradient.

	PSNR↑	SSIM↑	LPIPS↓
position	25.43	0.765	0.230
color($p = 0.2$)	25.47	0.770	0.216
color($p = 0.5$)	25.48	0.769	0.214
color($p = 0.9$)	25.53	0.771	0.213

Table 4. Ablation on Dilated Rendering for Bicycle [1].

	PSNR↑	SSIM↑	LPIPS↓
Full Resolution	25.51	0.770	0.216
Multi-scale	25.29	0.755	0.237
Dilated	25.47	0.770	0.216

policy achieves comparable SSIM and LPIPS scores as the full-resolution training policy.

6. Conclusion and Limitations

In this work, we present Turbo-GS, an efficient method that accelerates 3DGS model fitting by $5\times$ compared to previous methods. We propose two major design choices in the current optimization framework. First, we design an aggressive densification strategy that achieves faster optimization and requires fewer steps. Our densification strategy performs better than other methods in textured regions such as grass, floors, etc. Secondly, we introduce dilated rendering, which renders only a subset of the pixels rather than the entire image, allowing accelerated training on images exceeding 4K resolution while maintaining high quality. Our approach outperforms all existing methods in training time for standard 1K scenes while matching or surpassing their rendering quality. We also exceed baseline methods on existing 4K datasets. This paper aims at a learning-free design, thus lacking exploration on how to integrate with a geometry foundation model. With many such models gradually changing the entire community, we will consider how to benefit from a large model in the future to achieve further acceleration.

Acknowledgements

This research was supported by NASA grant #80NSSC23M0075, and NSF CAREER grant #2143576. Collaboration between Brown and IISc was facilitated through Kotak Mahindra Bank's Visiting Chair Professorship for Srinath. Ankit Dhiman was supported by Samsung R & D Institute India - Bangalore.

References

- [1] Jonathan T Barron, Ben Mildenhall, Dor Verbin, Pratul P Srinivasan, and Peter Hedman. Mip-nerf 360: Unbounded anti-aliased neural radiance fields. In *Proceedings of the IEEE/CVF conference on computer vision and pattern recognition*, pages 5470–5479, 2022. 1, 2, 5, 6, 7, 8, 3
- [2] David Charatan, Sizhe Lester Li, Andrea Tagliasacchi, and Vincent Sitzmann. Pixelsplat: 3d gaussian splats from image pairs for scalable generalizable 3d reconstruction. *2024 IEEE/CVF Conference on Computer Vision and Pattern Recognition (CVPR)*, pages 19457–19467, 2023. 3
- [3] Anpei Chen, Zexiang Xu, Andreas Geiger, Jingyi Yu, and Hao Su. Tensorf: Tensorial radiance fields. In *European conference on computer vision*, pages 333–350. Springer, 2022. 2
- [4] Anpei Chen, Haofei Xu, Stefano Esposito, Siyu Tang, and Andreas Geiger. Lara: Efficient large-baseline radiance fields. *ArXiv*, abs/2407.04699, 2024. 3
- [5] Yuedong Chen, Haofei Xu, Chuanxia Zheng, Bohan Zhuang, Marc Pollefeys, Andreas Geiger, Tat-Jen Cham, and Jianfei Cai. Mvsplat: Efficient 3d gaussian splatting from sparse multi-view images. *ArXiv*, abs/2403.14627, 2024. 3
- [6] Qiyu Dai, Yan Zhu, Yiran Geng, Ciyu Ruan, Jiazhao Zhang, and He Wang. Graspnerf: Multiview-based 6-dof grasp detection for transparent and specular objects using generalizable nerf. In *2023 IEEE International Conference on Robotics and Automation (ICRA)*, pages 1757–1763. IEEE, 2023. 2
- [7] Nianchen Deng, Zhenyi He, Jiannan Ye, Budmonde Duinkharjav, Praneeth Chakravarthula, Xubo Yang, and Qi Sun. Fov-nerf: Foveated neural radiance fields for virtual reality. *IEEE Transactions on Visualization and Computer Graphics*, 28(11):3854–3864, 2022. 2
- [8] Sankeerth Durvasula, Adrian Zhao, Fan Chen, Ruofan Liang, Pawan Kumar Sanjaya, and Nandita Vijaykumar. Distwar: Fast differentiable rendering on raster-based rendering pipelines. *ArXiv*, abs/2401.05345, 2023. 3
- [9] Zhiwen Fan, Kevin Wang, Kairun Wen, Zehao Zhu, De-jia Xu, and Zhangyang Wang. Lightgaussian: Unbounded 3d gaussian compression with 15x reduction and 200+ fps. *ArXiv*, abs/2311.17245, 2023. 3
- [10] Zhiwen Fan, Wenyan Cong, Kairun Wen, Kevin Wang, Jian Zhang, Xinghao Ding, Danfei Xu, B. Ivanovic, Marco Pavone, Georgios Pavlakos, Zhangyang Wang, and Yue Wang. Instantsplat: Unbounded sparse-view pose-free gaussian splatting in 40 seconds. *ArXiv*, abs/2403.20309, 2024. 3
- [11] Zhiwen Fan, Wenyan Cong, Kairun Wen, Kevin Wang, Jian Zhang, Xinghao Ding, Danfei Xu, Boris Ivanovic, Marco Pavone, Georgios Pavlakos, Zhangyang Wang, and Yue Wang. Instantsplat: Unbounded sparse-view pose-free gaussian splatting in 40 seconds, 2024. 2
- [12] Guangchi Fang and Bing Wang. Mini-splatting: Representing scenes with a constrained number of gaussians. *European Conference on Computer Vision*, 2024. 3, 7, 8, 2
- [13] Guofeng Feng, Siyan Chen, Rong Fu, Zimu Liao, Yi Wang, Tao Liu, Zhiling Pei, Hengjie Li, Xingcheng Zhang, and Bo Dai. Flashgs: Efficient 3d gaussian splatting for large-scale and high-resolution rendering. *ArXiv*, abs/2408.07967, 2024. 3
- [14] Yalda Foroutan, Daniel Rebain, Kwang Moo Yi, and Andrea Tagliasacchi. Evaluating alternatives to sfm point cloud initialization for gaussian splatting. 2024. 3
- [15] Sara Fridovich-Keil, Alex Yu, Matthew Tancik, Qinhong Chen, Benjamin Recht, and Angjoo Kanazawa. Plenoxels: Radiance fields without neural networks. In *Proceedings of the IEEE/CVF conference on computer vision and pattern recognition*, pages 5501–5510, 2022. 2, 3, 8
- [16] Sharath Girish, Kamal Gupta, and Abhinav Shrivastava. Eagles: Efficient accelerated 3d gaussians with lightweight encodings. *European Conference on Computer Vision*, 2024. 2, 3, 7, 8
- [17] Antoine Gu'edon and Vincent Lepetit. Sugar: Surface-aligned gaussian splatting for efficient 3d mesh reconstruction and high-quality mesh rendering. *2024 IEEE/CVF Conference on Computer Vision and Pattern Recognition (CVPR)*, pages 5354–5363, 2023. 3
- [18] Antoine Gu'edon and Vincent Lepetit. Sugar: Surface-aligned gaussian splatting for efficient 3d mesh reconstruction and high-quality mesh rendering. In *Proceedings of the IEEE/CVF Conference on Computer Vision and Pattern Recognition*, pages 5354–5363, 2024. 2
- [19] Peter Hedman, Julien Philip, True Price, Jan-Michael Frahm, George Drettakis, and Gabriel Brostow. Deep blending for free-viewpoint image-based rendering. *ACM Transactions on Graphics (ToG)*, 37(6):1–15, 2018. 6, 8, 1, 2, 3
- [20] Lukas H'ollein, Aljavz Bovzivc, Michael Zollhofer, and Matthias Nie'ßner. 3dgs-lm: Faster gaussian-splatting optimization with levenberg-marquardt. *ArXiv*, abs/2409.12892, 2024. 2, 3, 4
- [21] Binbin Huang, Zehao Yu, Anpei Chen, Andreas Geiger, and Shenghua Gao. 2d gaussian splatting for geometrically accurate radiance fields. *ArXiv*, abs/2403.17888, 2024. 3
- [22] Jaewoo Jung, Jisang Han, Honggyu An, Jiwon Kang, Seonghoon Park, and Seungryong Kim. Relaxing accurate initialization constraint for 3d gaussian splatting. *ArXiv*, abs/2403.09413, 2024. 3
- [23] Animesh Karnewar, Tobias Ritschel, Oliver Wang, and Niloy Jyoti Mitra. Relu fields: The little non-linearity that could. *ACM SIGGRAPH 2022 Conference Proceedings*, 2022. 3
- [24] Bernhard Kerbl, Georgios Kopanas, Thomas Leimk'uhler, and George Drettakis. 3d gaussian splatting for real-time radiance field rendering. *ACM Trans. Graph.*, 42(4):139–1, 2023. 2, 3, 4, 6, 7, 8

- [25] Bernhard Kerbl, Andr’eas Meuleman, Georgios Kopanas, Michael Wimmer, Alexandre Lanvin, and George Drettakis. A hierarchical 3d gaussian representation for real-time rendering of very large datasets. *ACM Trans. Graph.*, 43:62:1–62:15, 2024. 3
- [26] Shakiba Kheradmand, Daniel Rebain, Gopal Sharma, Weiwei Sun, Jeff Tseng, Hossam Isack, Abhishek Kar, Andrea Tagliasacchi, and Kwang Moo Yi. 3d gaussian splatting as markov chain monte carlo. *ArXiv*, abs/2404.09591, 2024. 3
- [27] Arno Knapitsch, Jaesik Park, Qian-Yi Zhou, and Vladlen Koltun. Tanks and temples: Benchmarking large-scale scene reconstruction. *ACM Transactions on Graphics (ToG)*, 36(4):1–13, 2017. 1, 2, 3
- [28] Zhengyang Liang, Hao He, Ceyuan Yang, and Bo Dai. Scaling laws for diffusion transformers. *arXiv preprint arXiv:2410.08184*, 2024. 5
- [29] Tao Lu, Mulin Yu, Linning Xu, Yuanbo Xiangli, Limin Wang, Dahua Lin, and Bo Dai. Scaffold-gs: Structured 3d gaussians for view-adaptive rendering. In *Proceedings of the IEEE/CVF Conference on Computer Vision and Pattern Recognition*, pages 20654–20664, 2024. 2, 3, 4, 5, 6, 7, 8
- [30] Mallick and Goel, Bernhard Kerbl, Francisco Vicente Carasco, Markus Steinberger, and Fernando De La Torre. Taming 3dgs: High-quality radiance fields with limited resources. In *SIGGRAPH Asia 2024 Conference Papers*, 2024. 2, 3, 4, 6, 7, 8
- [31] Ben Mildenhall, Pratul P. Srinivasan, Matthew Tancik, Jonathan T. Barron, Ravi Ramamoorthi, and Ren Ng. Nerf. *Communications of the ACM*, 65:99 – 106, 2020. 1, 2, 3
- [32] Thomas Müller, Alex Evans, Christoph Schied, and Alexander Keller. Instant neural graphics primitives with a multiresolution hash encoding. *ACM Transactions on Graphics (TOG)*, 41:1 – 15, 2022. 3
- [33] Thomas Müller, Alex Evans, Christoph Schied, and Alexander Keller. Instant neural graphics primitives with a multiresolution hash encoding. *ACM transactions on graphics (TOG)*, 41(4):1–15, 2022. 2, 8
- [34] K. L. Navaneet, Kossar Pourahmadi Meibodi, Soroush Abbasi Koohpayegani, and Hamed Pirsiavash. Compgs: Smaller and faster gaussian splatting with vector quantization. 2023. 3
- [35] Avinash Paliwal, Wei Ye, Jinhui Xiong, Dmytro Kotovenko, Rakesh Ranjan, Vikas Chandra, and Nima Khademi Kalantari. Coherentgs: Sparse novel view synthesis with coherent 3d gaussians. *ArXiv*, abs/2403.19495, 2024. 3
- [36] Panagiotis Papantonakis, Georgios Kopanas, Bernhard Kerbl, Alexandre Lanvin, and George Drettakis. Reducing the memory footprint of 3d gaussian splatting. *Proceedings of the ACM on Computer Graphics and Interactive Techniques*, 7:1 – 17, 2024. 3
- [37] Kerui Ren, Lihan Jiang, Tao Lu, Mulin Yu, Linning Xu, Zhangkai Ni, and Bo Dai. Octree-gs: Towards consistent real-time rendering with lod-structured 3d gaussians. *arXiv preprint arXiv:2403.17898*, 2024. 3
- [38] Johannes Lutz Schönberger, Enliang Zheng, Marc Pollefeys, and Jan-Michael Frahm. Pixelwise View Selection for Unstructured Multi-View Stereo. In *European Conference on Computer Vision (ECCV)*, 2016. 2
- [39] Cheng Sun, Min Sun, and Hwann-Tzong Chen. Direct voxel grid optimization: Super-fast convergence for radiance fields reconstruction. *2022 IEEE/CVF Conference on Computer Vision and Pattern Recognition (CVPR)*, pages 5449–5459, 2021. 3
- [40] Zhou Wang, Alan C Bovik, Hamid R Sheikh, and Eero P Simoncelli. Image quality assessment: from error visibility to structural similarity. *IEEE transactions on image processing*, 13(4):600–612, 2004. 6
- [41] Linning Xu, Yuanbo Xiangli, Sida Peng, Xingang Pan, Nanxuan Zhao, Christian Theobalt, Bo Dai, and Dahua Lin. Grid-guided neural radiance fields for large urban scenes. *2023 IEEE/CVF Conference on Computer Vision and Pattern Recognition (CVPR)*, pages 8296–8306, 2023. 3
- [42] Qiangeng Xu, Zexiang Xu, Julien Philip, Sai Bi, Zhixin Shu, Kalyan Sunkavalli, and Ulrich Neumann. Point-nerf: Point-based neural radiance fields. *2022 IEEE/CVF Conference on Computer Vision and Pattern Recognition (CVPR)*, pages 5428–5438, 2022. 3
- [43] Lior Yariv, Peter Hedman, Christian Reiser, Dor Verbin, Pratul P Srinivasan, Richard Szeliski, Jonathan T Barron, and Ben Mildenhall. Bakedgsdf: Meshing neural sdf for real-time view synthesis. In *ACM SIGGRAPH 2023 Conference Proceedings*, pages 1–9, 2023. 2
- [44] Vickie Ye, Ruilong Li, Justin Kerr, Matias Turkulainen, Brent Yi, Zhuoyang Pan, Otto Seiskari, Jianbo Ye, Jeffrey Hu, Matthew Tancik, and Angjoo Kanazawa. gsplat: An open-source library for gaussian splatting. *ArXiv*, abs/2409.06765, 2024. 3
- [45] Alex Yu, Ruilong Li, Matthew Tancik, Hao Li, Ren Ng, and Angjoo Kanazawa. Plenotrees for real-time rendering of neural radiance fields. In *Proceedings of the IEEE/CVF International Conference on Computer Vision*, pages 5752–5761, 2021. 2
- [46] Mulin Yu, Tao Lu, Linning Xu, Lihan Jiang, Yuanbo Xiangli, and Bo Dai. Gsdf: 3dgs meets sdf for improved rendering and reconstruction. *ArXiv*, abs/2403.16964, 2024. 3
- [47] Zehao Yu, Anpei Chen, Binbin Huang, Torsten Sattler, and Andreas Geiger. Mip-splatting: Alias-free 3d gaussian splatting. *2024 IEEE/CVF Conference on Computer Vision and Pattern Recognition (CVPR)*, pages 19447–19456, 2023. 3, 8, 2
- [48] Yanjie Ze, Ge Yan, Yueh-Hua Wu, Annabella Macaluso, Yuying Ge, Jianglong Ye, Nicklas Hansen, Li Erran Li, and Xiaolong Wang. Gnfactor: Multi-task real robot learning with generalizable neural feature fields. In *Conference on Robot Learning*, pages 284–301. PMLR, 2023. 2
- [49] Kai Zhang, Sai Bi, Hao Tan, Yuanbo Xiangli, Nanxuan Zhao, Kalyan Sunkavalli, and Zexiang Xu. Gs-irm: Large reconstruction model for 3d gaussian splatting. *ArXiv*, abs/2404.19702, 2024. 3
- [50] Kai Zhang, Sai Bi, Hao Tan, Yuanbo Xiangli, Nanxuan Zhao, Kalyan Sunkavalli, and Zexiang Xu. Gs-irm: Large reconstruction model for 3d gaussian splatting. *European Conference on Computer Vision*, 2024. 2
- [51] Richard Zhang, Phillip Isola, Alexei A Efros, Eli Shechtman, and Oliver Wang. The unreasonable effectiveness of

deep features as a perceptual metric. In *Proceedings of the IEEE conference on computer vision and pattern recognition*, pages 586–595, 2018. [6](#)

- [52] Chen Ziwen, Hao Tan, Kai Zhang, Sai Bi, Fujun Luan, Yicong Hong, Li Fuxin, and Zexiang Xu. Long-irm: Long-sequence large reconstruction model for wide-coverage gaussian splats, 2024. [2](#)

Turbo-GS: Accelerating 3D Gaussian Fitting for High-Quality Radiance Fields

Supplementary Material

7. Implementation Details

7.1. More Implementation Details

For all the dataset with a resolution below 4K, we train it for $10k$ iterations. The maximum budget is set to $300k$ or $500k$ for low resolution dataset, $700k$ for 4K and higher resolution dataset. The batched training is activated in the last 50 iterations, with a batch size of 4. We calculate the average loss for each batch. For the baseline Scaffold-GS, we use different anchor feature for the covariance and color to better decouple the learning of geometry and appearance. In the densification, we replace the chunk-based duplicate removal with `torch.unique()` which reduces both the peak memory and the runtime. Other settings we follow the Scaffold-GS.

7.2. Convergence-aware Budget Control

To enhance the adaptiveness of the training process based on convergence patterns, we propose a dynamic scheduling mechanism that modulates the budget for each stage according to the deviation between recent and historical trends. As illustrated in Algorithm 1, this approach implements two adaptations: it dynamically adjusts both the power law exponent and the final budget target. The power law exponent is tuned based on the convergence behavior in log space, while the final budget is automatically scaled up or down depending on the loss decline rate. This dual-adaptation strategy enables the scheduler to respond effectively to varying convergence dynamics while maintaining training stability. Fig. 8 shows that with the adaptive budget control, the final number of primitives are significantly reduced while the rendering quality keeps comparable, implying that the budget control helps to add the proper number of Gaussians. And, fewer number of Gaussians denote a faster training process.

8. More Experiments and Results

Per-scene Results Here we list the error metrics used in our evaluation in Sec.4 across all considered methods and scenes, as shown in Tab 5- 8. **drjohnson-playroom** [19] belongs to the deep blending dataset; **train-truck** come from the Tanks and Temple [27] dataset; **bicycle-boonsai** are from MipNeRF360 [1].

Dilated Rendering The effectiveness of the dilated rendering is illustrated in Fig 9. We profile the entire process during training on a 4K scene. With the dilated design, we

Algorithm 1 Adaptive Power Law Scheduling

Require: N, M : Numbers for initialization and final budget

Require: $steps$: Total steps

Require: $window_size$: Window for trend analysis

Require: t : Current step

Ensure: $B(t)$: Current scheduled value

```
1: Initialize EMA smoother with  $\alpha_{ema} = 0.1$ 
2: if  $\text{len}(\text{loss\_history}) \leq \text{warmup\_steps}$  then
3:   Use default power law with  $\alpha = 1.0$ 
4: else
5:   Smoothing and Base Trend:
6:   Compute smoothed losses:  $\text{ema}_t = \alpha_{ema} \cdot \text{loss}_t + (1 - \alpha_{ema}) \cdot \text{ema}_{t-1}$ 
7:   Fit in log space:  $\log(\text{ema\_losses}) \sim \alpha_{base} \cdot \log(\text{steps})$ 
8:    $\alpha_{base} \leftarrow$  Moving average of recent  $\alpha_{base}$  values
9:   Dynamic Range Adjustment:
10:   $\text{rate} \leftarrow -\frac{d \log(\text{ema\_losses})}{d \log(\text{steps})}$  in recent window
11:  if  $\text{rate} > 0.05$  then
12:     $M_{adaptive} \leftarrow \min(M_{adaptive} \cdot 1.1, M \cdot 1.5)$ 
13:  else if  $\text{rate} < -0.05$  then
14:     $M_{adaptive} \leftarrow \max(M_{adaptive} \cdot 0.9, M \cdot 0.5)$ 
15:  end if
16:  Adaptive Power Law:
17:   $\text{deviation} \leftarrow -\text{rate} - \alpha_{base}$ 
18:   $\alpha \leftarrow \alpha_{base} + 0.5 \tanh(\text{deviation})$ 
19:  Clip  $\alpha$  to  $[0.1, 2.0]$ 
20: end if
21: return  $N + \frac{(t^\alpha - 1)}{(100^\alpha - 1)} \cdot (M_{adaptive} - N)$ 
```

accelerate both the forward and backward process significantly.

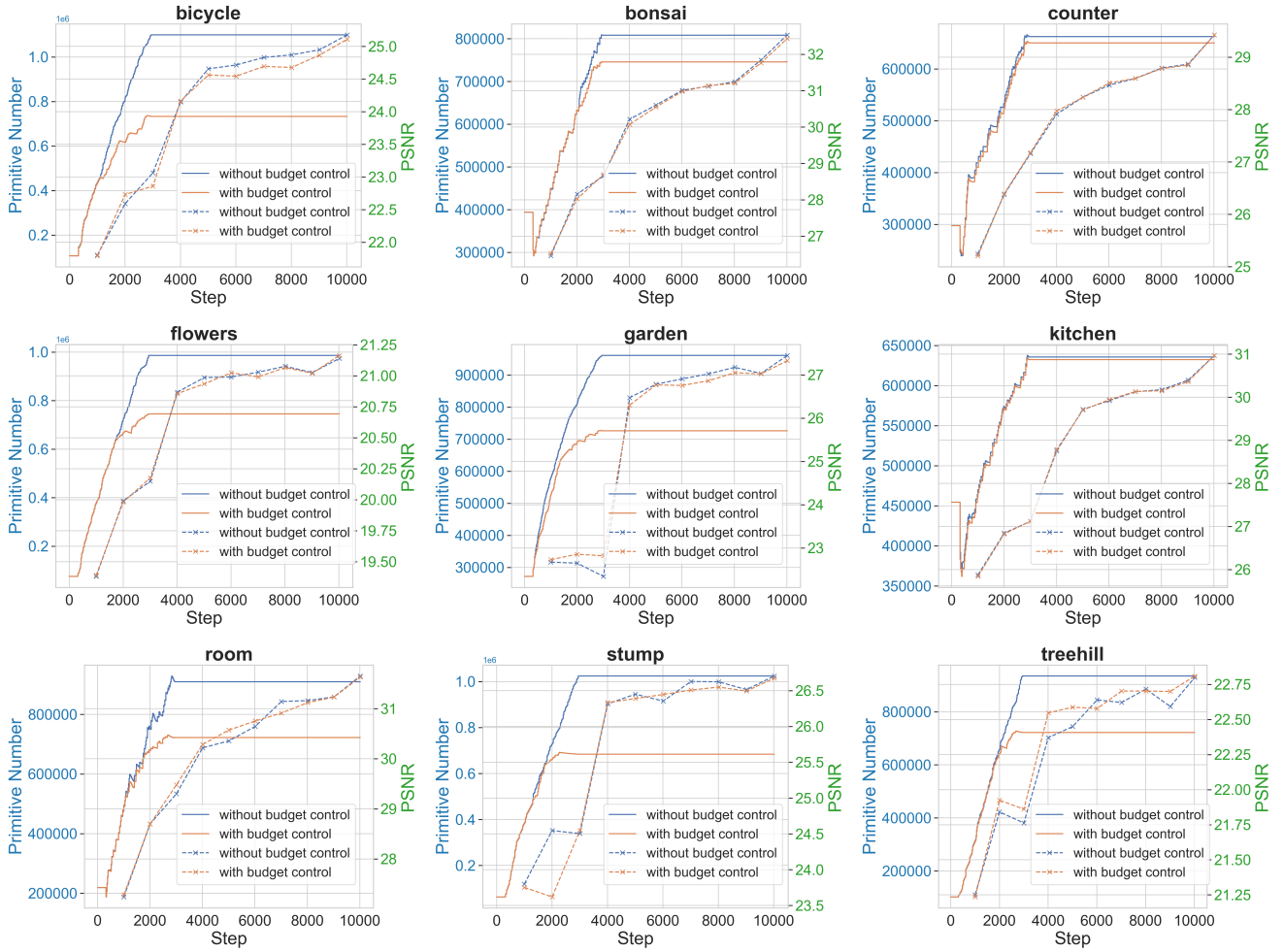


Figure 8. **Convergence.** We show “Number of primitives vs Step” and “PSNR vs Step” plots for scenes in MipNeRF-360 [1] dataset for with and without budget control in the optimization process. The proposed budgeting strategy prevents the number of primitives from increasing uncontrollably, while maintaining the overall quality. This is evident by the comparable PSNR plots, which demonstrate that the strategy maintains the balance between computational efficiency and visual fidelity.

Table 5. PSNR comparison across DeepBlending [19] (“drjohnson”, “playroom”), Tanks & Temples [27] (“train”, “truck”) and MipNeRF-360 [1] scenes.

Method	drjohnson	playroom	train	truck	bicycle	garden	stump	flowers	treehill	counter	kitchen	room	bonsai
3DGS [24]	29.49	30.02	22.11	25.45	25.23	27.38	26.59	21.44	22.49	29.08	31.09	31.48	32.31
Taming-3DGS [30]	29.39	30.04	22.09	25.46	25.22	27.35	26.62	21.50	22.59	29.07	30.98	31.62	32.22
Taming-3DGS* [30]	29.36	29.94	21.77	25.29	25.13	27.24	26.46	21.43	22.53	28.95	31.09	31.18	32.03
Mini-Splatting [12]	29.35	30.46	21.46	25.06	25.22	26.85	27.22	21.60	22.68	28.60	31.31	31.36	31.21
EAGLES [16]	29.35	30.19	21.36	25.00	24.97	26.87	26.61	21.31	22.62	28.30	30.52	31.38	31.23
ScaffoldGS [29]	29.67	30.90	22.53	25.86	25.21	27.51	26.56	21.43	23.12	29.45	31.61	31.98	32.53
Mip-Splatting [47]	28.75	29.98	22.06	25.74	25.56	27.69	26.91	21.70	22.35	29.13	31.59	31.54	32.27
Ours	29.69	31.12	21.31	25.67	25.01	27.43	26.41	21.12	22.75	29.22	30.96	31.23	32.29

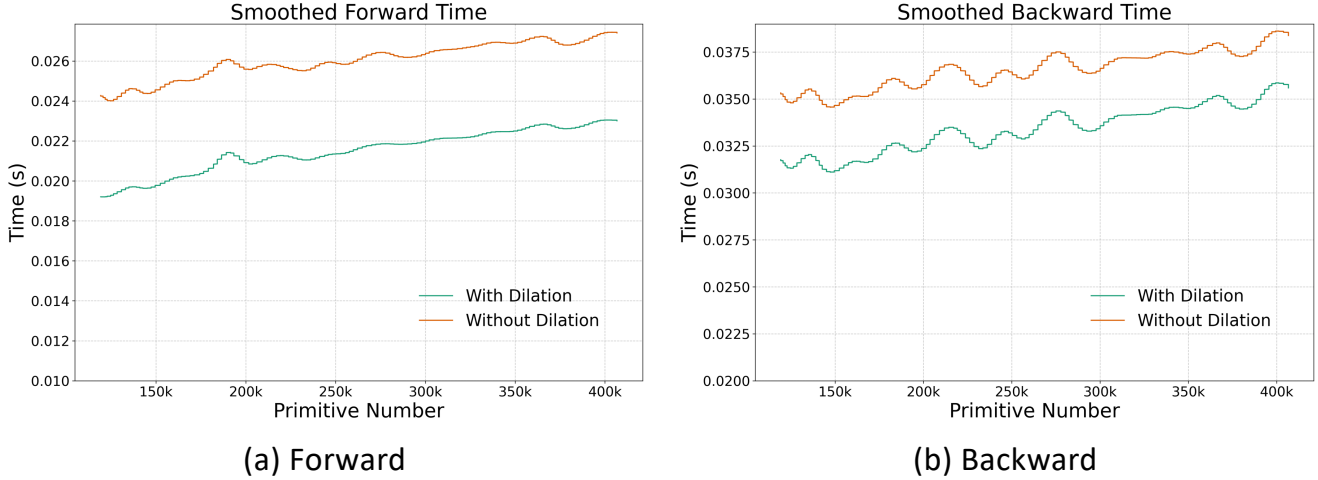


Figure 9. **Impact of Dilated Rendering on time performance.** We observe that dilated rendering significantly reduces the computational time required for both the (a) forward and (b) backward passes during the optimization process, compared to the without-dilated rendering approach. This highlights the efficiency of dilated rendering in accelerating the overall training process. The above results are shown for Bicycle from MipNeRF [1]. This enables Turbo-GS to achieve faster fitting for $\geq 4K$ scenes.

Table 6. SSIM comparison across DeepBlending [19] (“drjohnson”, “playroom”), Tanks & Temples [27] (“train”, “truck”) and MipNeRF-360 [1] scenes.

Method	drjohnson	playroom	train	truck	bicycle	garden	stump	flowers	treehill	counter	kitchen	room	bonsai
3DGS [24]	0.903	0.902	0.818	0.881	0.765	0.864	0.770	0.602	0.633	0.907	0.925	0.918	0.940
Taming-3DGS [30]	0.902	0.904	0.818	0.881	0.765	0.863	0.770	0.601	0.634	0.906	0.925	0.919	0.939
Taming-3DGS* [30]	0.903	0.901	0.812	0.878	0.751	0.859	0.764	0.596	0.630	0.905	0.923	0.915	0.939
Mini-Splatting [12]	0.903	0.912	0.798	0.874	0.773	0.848	0.806	0.626	0.654	0.905	0.926	0.922	0.939
EAGLES [16]	0.906	0.908	0.796	0.872	0.757	0.844	0.770	0.589	0.637	0.897	0.920	0.917	0.934
ScaffoldGS [29]	0.907	0.912	0.822	0.886	0.760	0.863	0.766	0.594	0.643	0.911	0.927	0.924	0.944
Mip-Splatting [47]	0.898	0.908	0.827	0.893	0.793	0.878	0.791	0.640	0.639	0.913	0.930	0.925	0.944
Ours	0.905	0.915	0.795	0.887	0.754	0.863	0.761	0.593	0.627	0.912	0.927	0.921	0.945

Table 7. LPIPS comparison across DeepBlending [19] (“drjohnson”, “playroom”), Tanks & Temples [27] (“train”, “truck”) and MipNeRF-360 [1] scenes.

Method	drjohnson	playroom	train	truck	bicycle	garden	stump	flowers	treehill	counter	kitchen	room	bonsai
3DGS [24]	0.238	0.243	0.198	0.143	0.211	0.108	0.217	0.339	0.329	0.201	0.127	0.220	0.205
Taming-3DGS [30]	0.239	0.243	0.200	0.144	0.210	0.109	0.217	0.341	0.328	0.202	0.127	0.219	0.206
Taming-3DGS* [30]	0.244	0.253	0.206	0.147	0.236	0.116	0.229	0.346	0.341	0.204	0.130	0.229	0.208
Mini-Splatting	0.256	0.249	0.245	0.160	0.225	0.150	0.199	0.327	0.313	0.198	0.129	0.211	0.200
EAGLES [16]	0.244	0.253	0.240	0.166	0.232	0.146	0.229	0.361	0.338	0.217	0.138	0.226	0.218
ScaffoldGS [29]	0.252	0.253	0.206	0.142	0.227	0.118	0.236	0.347	0.319	0.200	0.127	0.210	0.203
Mip-Splatting [47]	0.243	0.235	0.189	0.123	0.167	0.094	0.188	0.274	0.274	0.187	0.119	0.202	0.188
Ours	0.249	0.230	0.219	0.133	0.223	0.113	0.228	0.317	0.302	0.190	0.124	0.204	0.191

Table 8. Training time (in minutes) comparison across DeepBlending [19] (“drjohnson”, “playroom”), Tanks & Temples [27] (“train”, “truck”) and MipNeRF-360 [1] scenes.

Method	drjohnson	playroom	train	truck	bicycle	garden	stump	flowers	treehill	counter	kitchen	room	bonsai
3DGS	35.04	26.13	16.25	19.27	35.60	34.64	29.31	24.94	27.21	29.27	34.97	30.32	24.52
Taming-3DGS	15.71	11.02	8.11	11.74	22.58	22.31	18.88	14.65	15.37	11.44	15.51	11.35	9.92
Taming-3DGS*	9.40	6.81	6.22	7.51	11.95	12.72	9.17	8.35	8.53	9.37	14.52	8.28	7.60
Mini-Splatting	19.23	16.89	13.94	13.87	16.72	18.65	16.55	18.07	18.14	29.22	28.83	24.67	24.47
EAGLES	28.48	19.45	12.34	13.18	23.70	21.88	22.58	17.36	20.85	22.18	27.81	24.08	19.57
ScaffoldGS	17.64	16.87	15.02	14.68	22.41	23.99	18.08	21.05	21.14	27.32	32.84	23.41	24.42
Mip-Splatting	42.21	32.31	18.72	28.12	59.24	53.88	43.57	38.28	40.68	32.87	39.80	35.08	29.84
Ours	3.30	3.17	4.41	4.28	4.12	5.53	3.80	4.28	4.66	6.47	8.05	4.69	5.96